**World Scientific**
www.worldscientific.com

# A DIFFUSION–TRANSPORT HYBRID METHOD FOR ACCELERATING OPTICAL TOMOGRAPHY

HYUN KEOL KIM[*,§] and ANDREAS H. HIELSCHER[*,†,‡]

*Department of Biomedical Engineering
Columbia University, New York, NY 10027, USA

†Department of Radiology, Columbia University
New York, NY 10032, USA

‡Department of Electrical Engineering, Columbia University
New York, NY 10027, USA

§hkk2107@columbia.edu

It is well acknowledged that the equation of radiative transfer (ERT) provides an accurate prediction of light propagation in biological tissues, while the diffusion approximation (DA) is of limited accuracy for the transport regime. However, ERT-based reconstruction codes require much longer computation times as compared to DA-based reconstruction codes. We introduce here a computationally efficient algorithm, called a diffusion–transport hybrid solver, that makes use of the DA- or low-order ERT-based inverse solution as an initial guess for the full ERT-based reconstruction solution. To evaluate the performance of this hybrid method, we present extensive studies involving numerical tissue phantoms and experimental data. As a result, we show that the hybrid method reduces the reconstruction time by a factor of up to 23, depending on the physical character of the problem.

*Keywords*: Optical tomography; reconstruction time; radiative transfer equation.

## 1. Introduction

Diffuse optical tomography has emerged as a promising imaging modality that provides three-dimensional imaging of optical properties in biological tissue. Knowledge of such optical properties in tissue is very important for monitoring biological and physiological changes in tissue and for detecting various diseases long before the macroscopic symptoms appear. Thus this optical imaging technique has been mainly applied to breast imaging,[1–3] brain imaging,[4–8] finger-joint imaging,[9–11] and small animal studies.[12–15] This technique recovers the spatial distribution of optical properties in tissue from the outing radiation measured at boundary surfaces.

So-called model-based iterative image reconstruction algorithms (MOBIR)[16–26] are employed to find the optimal distribution of optical properties inside the medium, which requires a forward model of light propagation to predict the measured values on the boundary and the objective function that quantifies the difference between predicted and actually measured values.

In the past decades, the diffusion approximation (DA) to the equation of radiative transfer (ERT) was most commonly employed as a light propagation model in tissue optics. It is however well known that the DA becomes less accurate for the cases of high-absorbing, low-scattering media,

or small-tissue volumes, and is further compromised if fluid-filled regions, which contain cerebrospinal or synovial fluids, are considered.[27] These problems can be overcome by employing the ERT that provides accurate prediction of light propagation for all types of media. However, ERT-based reconstruction codes require much longer computation times as compared to DA-based reconstruction codes. Thus it remains a challenging problem to develop computationally efficient ERT-based reconstruction schemes since the reconstruction process requires a large number of repeated forward simulations that often lead to prohibitively long computing times.

In this work, we present a DA-ERT hybrid approach that makes use of the DA- and low-order ERT as a forward model of light propagation to obtain a better initial guess. This approach can be used to accelerate the ERT-based image reconstruction process while maintaining the reconstruction accuracy. To begin with a description of the method, we define here some terms: hereafter the term "low-order" in the ERT means an $S_2$ or $S_4$ order of the $S_N$ quadrature (i.e., discrete ordinates) method, and the term "conventional or full ERT" indicates an S8 quadrature ERT (not a hybrid scheme). The main idea behind this hybrid method is as follows: since the DA or low-order ERT is computationally much more efficient as compared to the full ERT, we start the reconstruction with these computationally inexpensive models to a certain level of the objective function. After that point we replace the DA or low-order ERT model by the full ERT and continue the reconstruction to full convergence. In this way the hybrid method can achieve an optimum of the spatial distribution of unknown parameters while taking a much smaller number of full-ERT-based function evaluations. Thus we can accelerate the full ERT-based reconstruction process by using the DA- and low-order ERT forward model.

In this work, we introduce two types of hybrid codes: one is the DA-based hybrid code that uses the DA model to obtain the intermediate solution, and the other is the low-order ($S_2$ or $S_4$) ERT-based hybrid code that uses the $S_2$ or $S_4$ ERT model to obtain the intermediate solution. In the following, we provide a detailed description of the new method and present numerical and experimental studies, with a focus on the code performance in terms of CPU time and accuracy, by comparing the results of

the hybrid code to those of the conventional ERT-based code.

## 2. Forward Problem

### 2.1. *Light propagation model*

In this work, we employ frequency domain data. In this case the light source is amplitude-modulated by frequencies in the range of 50 to 1,000 MHz, and demodulation and phase shift of the photon density waves in tissue are measured.

#### 2.1.1. *Equation of radiative transfer (ERT)*

The frequency-domain forward problem for light propagation in turbid media can be accurately modeled by the frequency-dependent equation of radiative transfer, given by Ref. 16:

$$\left[ \Omega \cdot \nabla + \mu_a + \mu_s + i\frac{\omega}{c} \right] I(\mathbf{r}, \Omega, \omega)$$
$$= \frac{\mu_s}{4\pi} \int_{4\pi} I(\mathbf{r}, \Omega', \omega)\Phi(\Omega' \to \Omega)d\Omega'$$
$$+ S_c(\mathbf{r}, \Omega, \omega), \tag{1}$$

where $i = \sqrt{-1}$, $\mathbf{r}$ and $\omega$ are the spatial position vector and the modulation frequency, respectively, $c$ is the speed of light in the medium and $\Omega$ is the direction of photon propagation. The positive functions $\mu_a(\mathbf{r})$ and $\mu_s(\mathbf{r})$ are the absorption and scattering coefficients [cm$^{-1}$], respectively, and the unknown quantity $I(\mathbf{r}, \Omega, \omega)$ is the complex-valued radiation intensity, defined at $\mathbf{r}$ as a radiant power per unit solid angle per unit area normal to the direction of propagation $\Omega$ modulation frequency $\omega$. The normalized scattering phase function $\Phi(\Omega' \to \Omega)$ is the probability that photons traveling in the direction $\Omega'$ scatter into direction $\Omega$. We use the Henyey–Greenstein phase function[28] that is commonly used in tissue optics as:

$$\Phi(\Omega' \to \Omega) = \frac{1 - g^2}{(1 + g^2 - 2g\cos\Theta)^{3/2}}, \tag{2}$$

where $\Theta$ is the angle between $\Omega$ and $\Omega'$ and $g$ is the anisotropy factor which measures how peaked the scattering is. In order to treat anisotropic scattering properly, we renormalize the phase function (2) according to the procedure of Kim and Charette.[25]

In this work we implemented a partially reflective boundary condition which allows us to consider the refractive index mismatch at the air–tissue interface as[29]:

$$I_b(\mathbf{r}_b, \Omega, \omega)|_{\mathbf{n}_b \cdot \Omega < 0} = I^0(\mathbf{r}_b, \Omega, \omega) + R(\Omega', \Omega)$$
$$\cdot I(\mathbf{r}_b, \Omega', \omega)|_{\mathbf{n}_b \cdot \Omega' > 0}, \quad (3)$$

where $R(\Omega', \Omega)$ is the reflectivity at Fresnel interface from direction $\Omega'$ to direction $\Omega$, $I_b^0(\mathbf{r}, \Omega, \omega)$ is the radiation intensity due to the external source function, and subscript $b$ denotes the boundary surface of the medium, while $\mathbf{n}_b$ is the unit normal vector pointing outwards from the boundary surface. The refraction index of the medium is fixed at 1.37 throughout this study. The spatial domain in Eq. (1) is discretized with an unstructured node-centered finite-volume method and the angular domain with the discrete ordinates formulation. The $S_N$ quadrature scheme is employed that fits well into the discrete ordinates method, which replaces the equation of radiative transfer by the set of $N(N+2)$ coupled discretized equations. The discretization equations for all control volumes form the linear equation given by $\mathbf{A}I = \mathbf{b}$, where the matrix $\mathbf{A}$ contains the coefficients resulting from discretization of Eq. (1) and the boundary condition comes into the vector $\mathbf{b}$ as a result of discretization on Eq. (3). The resulting algebraic equation $\mathbf{A}I = \mathbf{b}$ is solved iteratively for the complex-valued intensity $I(\mathbf{r}, \Omega, \omega)$ through a Generalized Minimal Residual (GMRES($n$)) solver,[30] where $n$ denotes the number of iterations after which a GMRES solver is restarted. The complex-valued detector function, which predicts the detector readings at boundary surfaces, is defined as

$$P_{\mathbf{r}_w} = \int_{\mathbf{n} \cdot \Omega > 0} T(\mathbf{r}_w, \Omega) I(\mathbf{r}_w, \Omega, \omega)(\mathbf{n} \cdot \Omega) d\Omega, \quad (4)$$

where $T(\mathbf{r}_w, \Omega)$ is the transmissivity from the medium into the air, $\mathbf{n}$ is the outward vector normal to the surface and $\mathbf{r}_w$ is the position vector of the detector.

### 2.1.2. *Diffusion approximation (DA)*

The light propagation in scattering-dominant (i.e., high-scattering and low-absorbing) media can be accurately described by the diffusion approximation (DA) that has been widely used in tissue optics. The frequency-domain version of the DA can be written as[16]

$$-\nabla \cdot D(\mathbf{r})\nabla U(\mathbf{r}, \omega) + \left(\mu_a + \frac{\omega}{c}i\right) U(\mathbf{r}, \omega)$$
$$= f(\mathbf{r}) \quad \text{in X}, \quad (5)$$
$$U(\mathbf{r}, \omega) + 2D(\mathbf{r})A\frac{\partial U(\mathbf{r}, \omega)}{\partial \mathbf{n}} = 0 \quad \text{in } \partial\text{X},$$

where $A$ is the correction coefficient with reflection due to mismatched refractive indices, $U(\mathbf{r}, \omega)$ and $D(\mathbf{r})$ are the radiation density and the diffusion coefficient given respectively as

$$U(\mathbf{r}, \omega) = \int_{4\pi} I(\mathbf{r}, \Omega, \omega)d\Omega \quad \text{and}$$
$$D(\mathbf{r}) = \frac{1}{3[\mu_a + (1-g)\mu_s]}. \quad (6)$$

We used the Robin-type boundary condition to take into account the photon leakage at the boundary surface. The boundary photon flux (4) can be rewritten for the diffusion approximation as

$$P_{\mathbf{r}_w} = -D(\mathbf{r}_w)\frac{\partial U(\mathbf{r}_w, \omega)}{\partial \mathbf{n}}. \quad (7)$$

As before, Eq. (5) is discretized in the spatial domain with an unstructured node-centered finite-volume method. After discretization of Eq. (5), we solve the resulting linear system $\mathbf{A}U = \mathbf{b}$ of algebraic equations by using the GMRES($n$) solver as before.

## 3. Optical Tomographic Inverse Problem

The inverse problem associated with the estimation of the spatial distributions of unknown functions $\mu_a(\mathbf{r})$ and $\mu_s(\mathbf{r})$, can be solved by minimizing the following real-valued objective function that quantifies the difference between the predictions and the measurements as:

$$\phi = \frac{1}{2}\sum_{d=1}^{ND}|p_d - z_d|^2 = \frac{1}{2}\sum_{d=1}^{ND}|Q_d y - z_d|^2, \quad (8)$$

where $z_d$ are the measurements at $\mathbf{r}_{d'} \cdot d = 1, \ldots, ND$ (number of detector-source pairs), $Q$ is the measurement operator which projects the solution vector $y = I$ or $U$ of either the ERT or the DA onto the predictions $p_d$ of the measurements. The objective function given by Eq. (8) is minimized by differentiating $\phi$ with respect to each of the unknown function $\mu = (\mu_a, \mu_s)$. The minimization is performed here with the limited memory version of *Broyden–Fletcher–Goldfarb–Shanno* (lm-BFGS)[31]

in combination to an adjoint formulation[32] as described next.

Differentiating the objective function with optical properties $\mu = (\mu_a, \mu_s)$ is straightforward and leads to the following

$$\frac{\partial \phi}{\partial \mu} = \left[\sum_{d=1}^{ND} (\overline{Qy - z})Q\frac{\partial y}{\partial \mu}\right]_{\text{Re}}, \qquad (9)$$

where $[\cdot]_{\text{Re}}$ denotes the real part of $[\cdot]$ and the symbol $\overline{\mathbb{F}}$ represents the complex conjugate of $\mathbb{F}$. Note that the discretized version of the forward model (be it the DA or the ERT) can be expressed in general terms as a following complex-valued linear algebraic equation:

$$\mathbf{A}y = \mathbf{b}, \qquad (10)$$

where $\mathbf{A}$ are the coefficient matrix resulting from discretization on either the DA or the ERT. The boundary condition (with a source function) comes into $\mathbf{b}$. Also differentiation of Eq. (10) with respect to the inverse variable $\mu$ gives

$$\frac{\partial \mathbf{A}}{\partial \mu}y + \mathbf{A}\frac{\partial y}{\partial \mu} = 0, \qquad (11)$$

which leads to the following sensitivity coefficient as

$$\frac{\partial y}{\partial \mu} = -\mathbf{A}^{-1}\frac{\partial \mathbf{A}}{\partial \mu}y, \qquad (12)$$

since $\mathbf{A}$ is invertible. We thus have for the gradient of the objective function

$$\frac{\partial \phi}{\partial \mu} = \left[-\sum_{d=1}^{ND} (\overline{Qy - z})Q\mathbf{A}^{-1}\frac{\partial \mathbf{A}}{\partial \mu}y\right]_{\text{Re}}. \qquad (13)$$

Introducing a new variable $\boldsymbol{\lambda}$ called an adjoint variable gives the following equation

$$-\sum_{d=1}^{ND} (\overline{Qy - z})Q\mathbf{A}^{-1} = \boldsymbol{\lambda}^T, \qquad (14)$$

where $\boldsymbol{\lambda}^T$ denotes the transpose of $\boldsymbol{\lambda}$. The adjoint variable vector $\boldsymbol{\lambda}$ is the solution of the following *adjoint* equation of Eq. (15) given as

$$\mathbf{A}^T\boldsymbol{\lambda} = -\left[\sum_{d=1}^{ND} (\overline{Qy - z})Q\right]^T. \qquad (15)$$

By substituting Eq. (14) into Eq. (13), we arrive at the following form for the gradient of the objective function with respect to the optical properties

$$\frac{\partial \phi}{\partial \mu} = \left[\boldsymbol{\lambda}^T\frac{\partial \mathbf{A}}{\partial \mu}y\right]_{\text{Re}}, \qquad (16)$$

which is very crucial for updating the inverse variables in the iterative procedure of reconstruction.

## 4. Hybrid Methods

As described in the preceding section, we minimize the objective function by iteratively updating the optical parameters as:

$$\mu^{k+1} = \mu^k + \alpha^k d^k, \qquad (17)$$

where the superscript $k$ is the iteration number; $\alpha$ and $d$ are the search step size and the direction of descent, respectively. We employed here the lm-BFGS method as an updating scheme that has been known to be the most efficient unconstrained gradient-based method among other gradient-type methods (e.g., conjugate gradient method) used in the optical imaging field. In the following, we present a detailed description of two hybrid algorithms with the lm-BFGS updating scheme: the DA-based hybrid scheme and the low-order ERT-based hybrid scheme.

### 4.1. *DA-based hybrid scheme*

In the DA-based hybrid method, the reconstruction is performed in two steps: first, the DA is used as a light propagation model until this DA-based reconstruction satisfies the prescribed stopping criterion. Next, the full ERT replaces the DA model and uses the DA-based inverse solution $\mu^m$ as the initial guess for the full ERT-based reconstruction. In this way, we reach the optimum with less CPU times as compared to the conventional ERT-based code that uses the full ERT alone throughout the optimization process. A brief summary of this algorithm is as follows:

(1) Pick up a homogeneous initial guess $\mu^0$ and set $k = 0$.
(2) Intermediate solution through the DA-based reconstruction:

   (A) Solve the DA (5) for $U(\mathbf{r}, \omega)$, based on $\mu^k$.
   (B) Check the stopping criterion with a loose tolerance. Continue if not satisfied.
   (C) Knowing detector predictions $p_d$ and detector readings $z_d$, solve the adjoint problem (15) for $\boldsymbol{\lambda}$ and compute $\nabla\phi[\mu]$ from (16).
   (D) Knowing the gradients $\nabla\phi$, update the unknowns $\mu^{k+1}$ from the lm-BFGS method, and return to Step (2)A.

(3) Set the intermediate solution $\mu^m$ as the new initial guess $\mu^0$:

    (A) Solve the ERT (1) for $I(\mathbf{r}, \Omega, \omega)$, based on $\mu^k$.

    (B) Check the stopping criterion with a tight tolerance. Continue if not satisfied.

    (C) Knowing detector predictions $p_d$ and detector readings $z_d$, solve the adjoint problem (15) for $\boldsymbol{\lambda}$ and compute $\nabla\phi[\mu]$ from (16).

    (D) Knowing the gradients $\nabla\phi$, update the unknowns $\mu^{k+1}$ from the lm-BFGS method, and return to Step (3)A.

(4) Terminate the optimization process.

## 4.2. *Low-order ERT-based hybrid scheme: LOERT-H*

As mentioned earlier, the DA is of limited accuracy as a light propagation model when high-absorbing, low-scattering or fluid-filled (i.e., void-like) regions are considered. In this case, the DA-based reconstruction does not perform well to make the good initial guess for the full ERT-based reconstruction. As an alternative for such cases, we use here the low-order (i.e., $S_2$ or $S_4$) ERT as the forward model for the intermediate solution $\mu^m$. As compared to the DA, this low-order ERT requires a longer CPU time but is still much less expensive than the full ERT. For examples, the $S_2$ ERT is for only four angular directions while the $S_8$ ERT is for 80 angular directions. It is quite easy to see that the CPU time for the $S_2$ ERT solution reduces to one-tenth of the CPU time for the $S_8$ ERT solution, which leads to lots of time savings when this low-order ERT is combined into the reconstruction. Moreover, unlike the DA, the low-order ERT can be applied to the types of media with high-absorbing or void-like regions. Hence, we employ in this work the low-order ERT as an initial guessing tool in the hybrid scheme.

Similar to the DA-based hybrid scheme, the low-order ERT-based hybrid scheme first obtains the intermediate solution $\mu^m$ through the low-order ERT-based reconstruction and uses $\mu^m$ as an initial guess for the full ERT-based reconstruction. This algorithm that is similar to the DA-based hybrid scheme has the following structure scheme:

(1) Pick up a homogeneous initial guess $\mu^0$ and set $k = 0$.

(2) Intermediate solution through the low-order ERT-based reconstruction:

    (A) Solve the transport Eq. (1) with the $S_2$ (or $S_4$) transport theory for $I(\mathbf{r}, \Omega, \omega)$, based on $\mu_k$.

    (B) Check the stopping criterion. Continue if not satisfied.

    (C) Knowing detector predictions $p_d$ and detector readings $z_d$, solve the adjoint problem (14) for $\boldsymbol{\lambda}(x, y, \Omega, \omega)$ and compute $\nabla\phi[\mu]$ from (15).

    (D) Knowing the gradients $\nabla\phi$, update the unknowns $\mu^{k+1}$ from the lm-BFGS method, and return to Step (2)A.

(3) Set the intermediate solution $\mu^k$ as the new initial guess $\mu^0$:

    (E) Solve the transport Eq. (1) with the higher-order (full) transport theory for $I(\mathbf{r}, \Omega, \omega)$, based on $\mu^k$.

    (F) Check the strong stopping criterion below (23). Continue if not satisfied.

    (G) Knowing detector predictions $P_d$ and detector readings $M_d$, solve the adjoint problem (15) for $\boldsymbol{\lambda}(x, y, \Omega, \omega)$ and compute $\nabla\phi[\mu]$ from (16).

    (H) Knowing the gradients $\nabla\phi$, update the unknowns $\mu^{k+1}$ from the lm-BFGS method, and return to Step (3)A.

(4) Stop the optimization process.

## 4.3. *Stopping criteria*

In both of the two hybrid schemes, we stop the optimization process when the following stopping criteria are satisfied:

$$\phi(\mu^{k+1}) < \varepsilon_t,$$
$$|1 - \phi(\mu^{k+1})/\phi(\mu^k)| < 10^{-3}, \tag{18}$$

where the prescribed tolerance $\varepsilon_t$ is chosen to have the same order of magnitude of the measurement error, which leads to sufficiently stable results in the principle of discrepancy.[32] When noise-free data are used, the tolerance $\varepsilon_t$ is assigned a very small number (typically $10^{-6}$). The stopping criteria given by Eq. (18) are applied in the same way to the DA-based and low-order ERT-based hybrid methods.

We use the same stopping criteria (18) with a loose tolerance for the intermediate solution $\mu^m$ by either the DA-based or the low-order ERT-based reconstruction. The reason for this choice with a loose tolerance is because the attempts to full convergence could give rise to worse intermediate solutions when both DA- and low-order ERT-based

codes are of limited accuracy. Note that the DA and the low-order ($S_2$ or $S_4$) ERT become inaccurate for the transport regime and for highly anisotropic scattering media, respectively.

## 5.   Results and Discussions

### 5.1.   *Numerical experiments*

In this section, we present numerical results of reconstructions of the spatial distributions of optical properties inside the medium by using the hybrid schemes. To evaluate the performance of the hybrid schemes, we compare the results of the schemes on various test problems, all with circular enclosures.

As shown in Fig. 1, the test medium has two objects embedded in the background: one with inhomogeneity in the absorption coefficient and the other with inhomogeneity in the scattering coefficient. The circular enclosure is centered at $(0, 0)$ and eight sources are located around the enclosure surface at equiangular intervals. The sources are amplitude-modulated with a frequency of 400 MHz, and are zero-phased so that the phases measured at detectors could directly represent the phase delay to the sources. The 56 detectors are equally spaced around the enclosure surface. This yields a total of 448 source–detector pairs for reconstruction. The optical properties of the background medium are varied depending on each case of the problems, all within the transport regime. See Table 1 for a detailed setup of the problem and the corresponding optical properties of the background medium and the target object. For the numerical experiments, we used the synthetic data: we first calculated the

predictions of the measurements at specified detector locations by solving the ERT for a given set of optical properties for each of the problems, and added random noise of 15 dB to the exact "noisy-free" data. Note that all synthetic data are generated on a mesh that is two times finer than the mesh used for the reconstructions. To quantify the reconstruction quality, we use two metrics called a correlation factor $\rho(\mu^e, \mu^r)$ and a deviation factor $\delta(\mu^e, \mu^r)$, as introduced in Ref. 21:

$$\rho(\mu^e, \mu^r) = \frac{\sum_{i=1}^{N_t} (\mu_i^e - \bar{\mu}_i^e)(\mu_i^r - \bar{\mu}_i^r)}{(N_t - 1)\sigma(\mu^e)\sigma(\mu^r)},$$

$$\delta(\mu^e, \mu^r) = \frac{\sqrt{\sum_{i=1}^{N_t} (\mu_i^e - \mu_i^r)^2 N_t}}{\sigma(\mu^e)}, \tag{19}$$

where $\bar{\mu}$ and $\sigma(\mu)$ are the mean value and the standard deviation for the spatial function of the optical property that can be either the absorption coefficient or the scattering coefficient. Similarly, $\mu^e$ and $\mu^r$ are the exact and reconstructed distributions of optical properties, respectively. In terms of quality of the reconstruction results, $\rho(\mu^e, \mu^r)$ indicates the degree of correlation between exact and estimated quantities while $\delta(\mu^e, \mu^r)$ describes the discrepancy in absolute values of exact and estimated quantities. Accordingly, the closer $\rho(\mu^e, \mu^r)$ gets to unity, and the closer $\delta(\mu^e, \mu^r)$ gets to zero, the better is the quality of reconstruction. In the following, the two hybrid methods are applied to functional estimations of unknown optical properties for the three test cases. All the simulations are carried out on a Linux workstation with a 700-MHz Pentium Xeon processor. Note that the full ERT-based reconstruction is carried out with an $S_8$ angular quadrature.
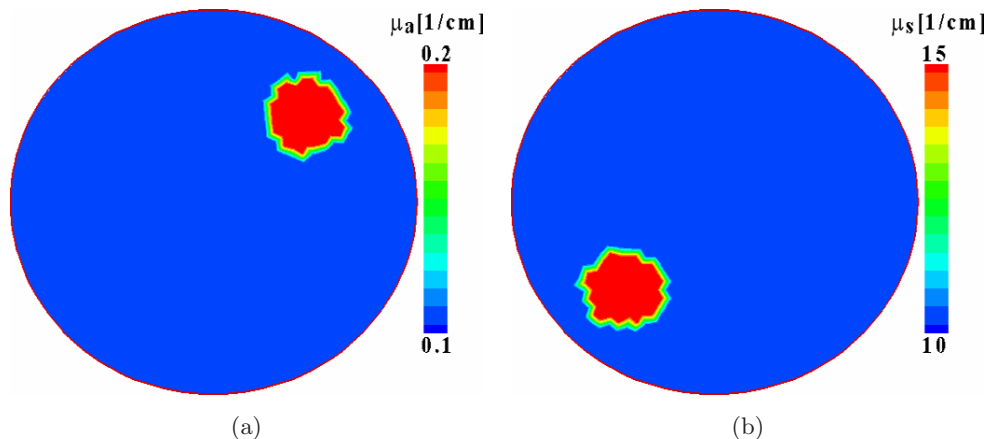


Fig. 1.    Numerical models used for reconstruction of optical properties in the 2 cm-in-diameter circular enclosure. (a) Target medium of inhomogeneity in the absorption coefficient. (b) Target medium of inhomogeneity in the scattering coefficient.

Table 1.   Problem setup and optical properties considered.

| Case | Enclosure size, $D$[cm] | Background $\mu_a$[cm$^{-1}$] | Background $\mu_s'$[cm$^{-1}$] | | Object $\mu_a$[cm$^{-1}$] | Object $\mu_s'$[cm$^{-1}$] |
|------|------|------|------|------|------|------|
| 1 | 2 | 0.1 | 10 | $g = 0.0$ | 0.2 | 10 |
| 2 | 2 | 0.1 | 7.5 | $g = 0.5$ | 0.2 | 7.5 |
| 3 | 2 | 0.1 | 5.0 | $g = 0.9$ | 0.2 | 5.0 |
| 4 | 2 | 0.1 | 10 | $g = 0.5$ | 0.1 | 15 |
| 5 | 4.2 | 0.023 | 7.5 | $g = 0.7$ | 0.4 | 7.5 |

First, we consider the simple, isotropic-scattering (i.e., $g = 0$) medium with inhomogeneity in the absorption coefficient (Case 1): it has a single object of $\mu_a = 0.2\,\text{cm}^{-1}$ embedded in the background as shown in Fig. 1(a). We retrieve the spatial distribution of absorption coefficients inside the medium by using the four reconstruction schemes: the conventional ERT-based reconstruction scheme, the DA-based hybrid scheme, and the $S_2$ and $S_4$ ERT-based hybrid schemes. The homogeneous initial guess is assumed for all the reconstruction schemes, and the reconstruction results are shown in Fig. 2. The measures of $\rho$ and $\delta$ and CPU times are given with the number of function evaluations in Table 2 for each of the methods. As expected, the four methods gave very similar results: the location of the object is well identified and the absolute values of the absorption coefficient are accurately reconstructed. In terms of the CPU time, however, we found that the hybrid schemes converge much faster than the conventional ERT-based reconstruction scheme. In more details, the DA-based hybrid scheme reached convergence after 46 function evaluations with the DA (taking 129 s) plus additional three function evaluations with the full ERT (taking 821 s). The $S_2$ ERT-based hybrid scheme took 54 forward runs with the $S_2$ ERT (1,532 s) plus additional five forward runs with the $S_8$ ERT (1,345 s). The $S_4$ ERT-based hybrid scheme converged after 47 function evaluations with the $S_4$ ERT (2,578 s) plus additional two function evaluations with the $S_8$ ERT (742 s). The conventional ERT-based reconstruction scheme reached convergence after a larger number of function evaluations, i.e., 92 forward runs taking 21,520 seconds.

Thus the DA-based hybrid scheme reduces the reconstruction time by a factor of 23, and the $S_2$ ($S_4$) ERT-based hybrid scheme leads to the factors of 7.4 (6.2), respectively. It can also be noted that among the three hybrid schemes, the accuracy is the highest for the $S_4$ ERT-based hybrid scheme and the CPU time taken is the smallest for the DA-based hybrid scheme. Figure 3 shows the convergence characteristics of the hybrid schemes as compared to the conventional ERT-based reconstruction scheme. It can be clearly seen from the figures that the DA- (and low-order ERT-) based hybrid codes lead to a significant improvement in the convergence rate. This fact demonstrates that for such a medium as Case 1 (with the optical properties given in Table 2), the DA (or low-order ERT) can be used as a forward model of light propagation
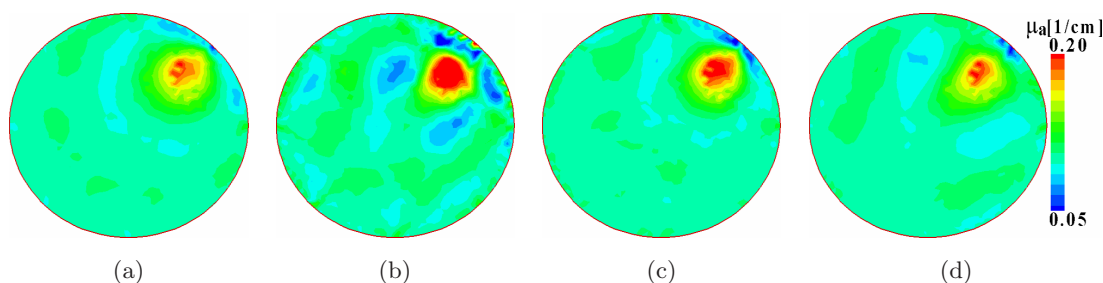


Fig. 2.   Case 1: Reconstruction results of the hybrid schemes compared with those with the full ERT-based scheme alone. (a) The DA-based hybrid scheme. (b) The $S_2$ ERT-based hybrid scheme. (c) The $S_4$ ERT-based hybrid scheme. (d) The full ERT-based conventional reconstruction code.

Table 2.  Reconstruction quality for the test cases obtained with the three proposed hybrid schemes; a small deviation and large correlation factor represents a high image quality.

| Case | Method | Forward runs | Time[sec.] | Correlation factor $E_c$ | Deviation factor $E_d$ |
|---|---|---|---|---|---|
| 1 | full ERT | 82 | 21520 | 0.80 | 0.61 |
|  | diffusion+ERT | 46+3 | 950(=129+821)(**23**) | 0.80(0.74*) | 0.59(0.67*) |
|  | s2+ERT | 54+5 | 2877(=1532+1345)(**7.4**) | 0.79(0.75*) | 0.60(0.67*) |
|  | s4+ERT | 47+2 | 3320(=2578+742)(**6.2**) | 0.81(0.79*) | 0.59(0.61*) |
| 2 | full ERT | 71 | 19185 | 0.81 | 0.62 |
|  | diffusion+ERT | 33+13 | 3922(=110+3812)(**4.9**) | 0.79(0.63*) | 0.64(0.77*) |
|  | s2+ERT | 51+39 | 12059(=1521+10538)(**1.5**) | 0.72(0.51*) | 0.81(0.89*) |
|  | s4+ERT | 48+5 | 5733(=4382+1351)(**3.3**) | 0.81(0.78*) | 0.61(0.6*) |
| 3 | full ERT | 25 | 16943 | 0.83 | 0.56 |
|  | diffusion+ERT | F | F | F | F |
|  | s2+ERT | F | F | F | F |
|  | s4+ERT | 11+10 | 9150(=2438+6712)(**2.0**) | 0.84(0.75*) | 0.59(0.68*) |
| 4 | full ERT | 23 | 8395 | 0.80 | 0.64 |
|  | diffusion+ERT | 43+3 | 1415(=320+1095)(**7.6**) | 0.81(0.78*) | 0.65(0.63*) |
|  | s2+ERT | F | F | F | F |
|  | s4+ERT | 20+2 | 1694(=952+742)(**5.44**) | 0.81(0.81*) | 0.64(0.69*) |
| 5 | full ERT | 78 | 28783 | 0.84 | N/A |
|  | diffusion+ERT | 31+9 | 3787(=298+3489)(**7.6**) | 0.82(0.78*) | N/A |
|  | s2+ERT | F | F | F | N/A |
|  | s4+ERT | 26+6 | 5582(=3269+2313)(**5.2**) | 0.85(0.80*) | N/A |

*Note*: The letter F represents that either the DA or the low-order ERT does not improve the speed of reconstruction at all. The symbol "+" denotes the additional computational time (or function evaluations) required for the full ERT reconstruction in the hybrid reconstruction procedure. The symbol * denotes the accuracies with DA, $S_2$ or $S_4$ solutions. The bold numbers in parentheses denote the speedup factors by the hybrid schemes.

to find a good initial guess for the full ERT-based reconstruction.

Next, we reconsider the previous case by increasing the anisotropic factor $g$ and by decreasing the scattering coefficient $\mu'_s$ slightly. Two cases are considered: one with $g = 0.5$ and $\mu'_s = 7.5\,\mathrm{cm}^{-1}$ (Case 2) and one with $g = 0.9$ and $\mu'_s = 5.0\,\mathrm{cm}^{-1}$ (Case 3). With these examples we examine how well the DA and low-order ERT codes fit into such cases. The absorption coefficients for the background and the target object are kept the same as those in Case 1. As before, we reconstructed the absorption coefficient, and the accuracy of the results is given in Table 2 in terms of the correlation ($\rho$) and deviation ($\delta$) factors. Although all the methods gave similar accuracy for these two cases, a difference can be observed in the performance between the three hybrid schemes.

For the case with $g = 0.5$ (Case 2), the DA-based hybrid scheme took 33 forward runs (110 s) with the DA plus additional 13 forward runs (3,812 s) with the $S_8$ ERT. The $S_2$ ERT-based hybrid scheme converged after 51 forward runs (1,521 s) with the $S_2$ ERT plus additional

39 forward runs (10,538 s) with the $S_8$ ERT. The $S_4$ ERT-based hybrid scheme reached convergence after 48 function evaluations (4,382 s) with the $S_4$ ERT and additional five function evaluations (1,351 s) with the $S_8$ ERT. Thus the DA- and $S_4$ ERT-based schemes still work well, reducing the total reconstruction time, while as shown in Fig. 4 the $S_2$ ERT-based hybrid code does not seem to work well in this case, i.e., it does not improve the speed of reconstruction [see also Fig. 3(b)]. The reason for this can be explained by the fact that the $S_2$ ERT considers only eight angular directions to simulate an anisotropic scattering behavior with $g = 0.5$, and thus the $S_2$ quadrature is too coarse to capture the anisotropic scattering pattern properly. It should also be noted that among the three hybrid codes the $S_4$ ERT-based hybrid code gives the highest correlation factor $\rho$ (0.79) and the smallest deviation factor $\delta$ (0.63) for this case.

For Case 3, we observed that only the $S_4$ ERT-based code produces the feasible intermediate solution $\mu^m$ while the DA- and $S_2$ ERT-based codes do not converge to any reasonable solution [see Fig. 3(c) and Fig. 4]. In terms of function
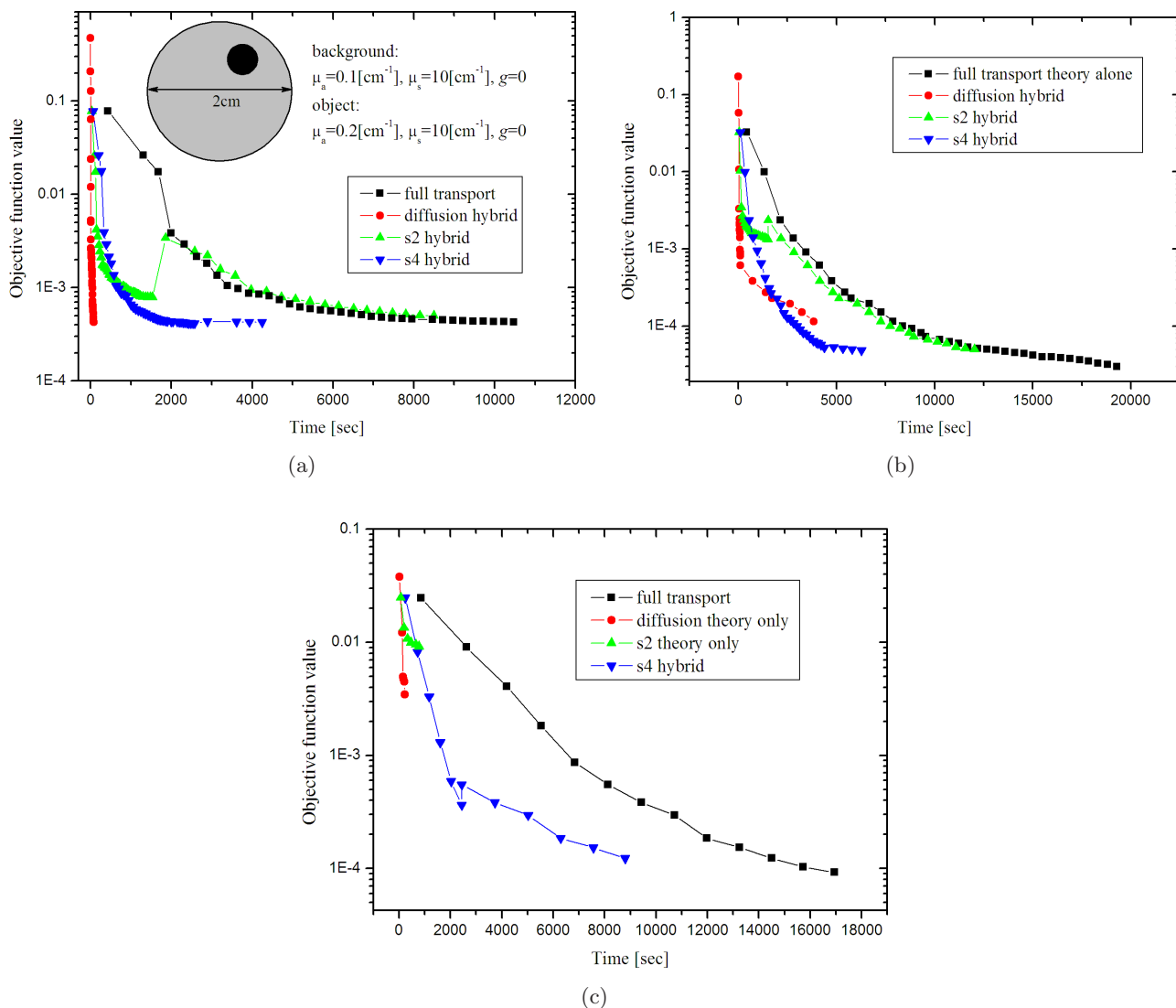
Fig. 3. Convergence characteristics of the hybrid schemes applied to the reconstruction of the spatial distribution of the absorption coefficient within the test medium. (a) Case 1. (b) Case 2. (c) Case 3.

evaluations, the $S_4$ ERT-based hybrid code took 11 function evaluations with the $S_4$ ERT (2,438 s) plus additional 10 function evaluations with the $S_8$ ERT (6,712 s), which consequently leads to a speedup factor of only two. The reason for this observation can be understood by looking at the fact that this case with $g = 0.9$, $\mu_a = 0.1\,\text{cm}^{-1}$ and $\mu_s' = 5.0\,\text{cm}^{-1}$ is far from the diffuse regime and thus can be considered to be closer to the transport regime. That is why the DA and $S_2$ ERT models fail for this case. As a result, for the low-scattering, high-anisotropic cases, it can be stated that the performance of the hybrid codes on the speedup of reconstruction is not significant as compared to the two previous cases.

Next, we consider the case of reconstructing the scattering coefficient $\mu_s'$ inside the medium (Case 4). The absorption and scattering coefficients of the background medium are the same as for Case 1 and the anisotropic factor $g$ is set to 0.5 as Case 2. The target object has inhomogeneity in $\mu_s'$ as shown in Fig. 1(b) (see Table 1). The three hybrid schemes are applied to the estimation of the spatial distribution of the scattering coefficient $\mu_s'$ inside the medium, and then the results were compared to those of the full ($S_8$) ERT-based code in terms of CPU time and accuracy. The CPU times and accuracy for this case are also summarized in Table 2 for all the codes used. Also the intermediate solutions $\mu^m$ are displayed in Fig. 5 for each of the hybrid codes. As a result, it was shown that the $S_2$ ERT-based code did not give satisfactory results for the intermediate solution $\mu^m$ for the
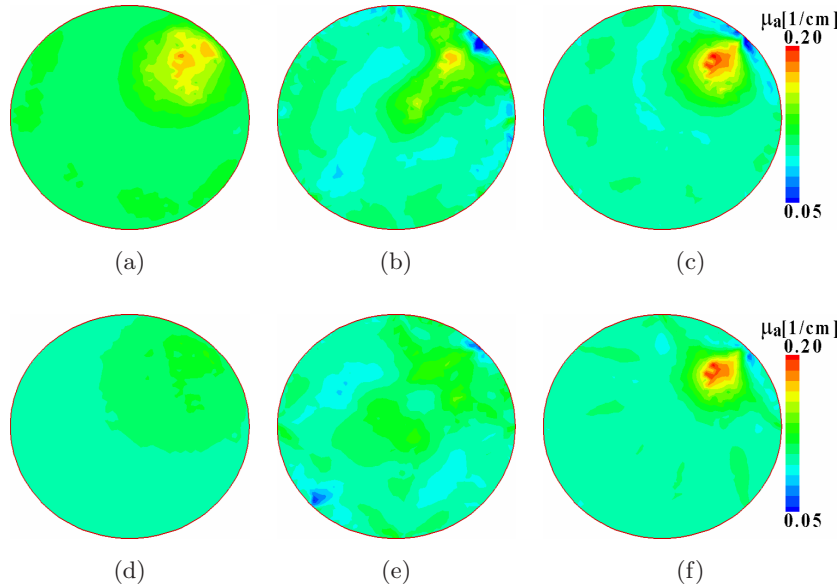
Fig. 4.   Intermediate inverse solutions for Case 2 obtained with: (a) DA; (b) $S_2$ ERT; (c) $S_4$ ERT, and for Case 3 obtained with: (d) DA; (e) $S_2$ ERT; (f) $S_4$ ERT.
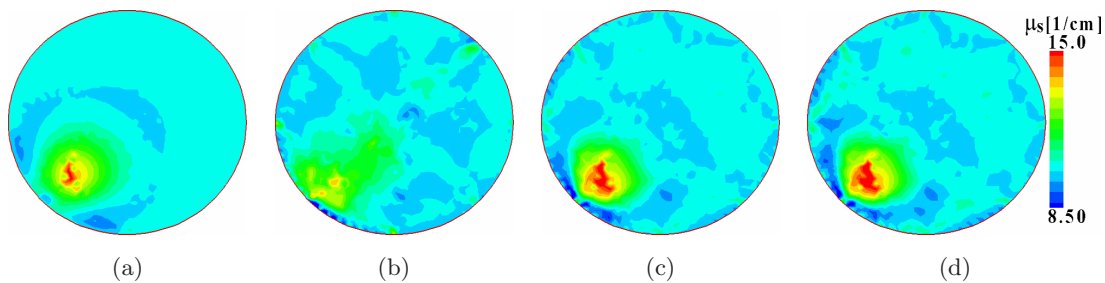


Fig. 5.   Intermediate inverse solutions for Case 4 obtained with: (a) the DA-based reconstruction; (b) the $S_2$ ERT-based reconstruction; (c) the $S_4$ ERT-based reconstruction. Compare the intermediate solutions (a), (b) and (c) to the reconstruction results (d) by the full ERT-based conventional reconstruction method.
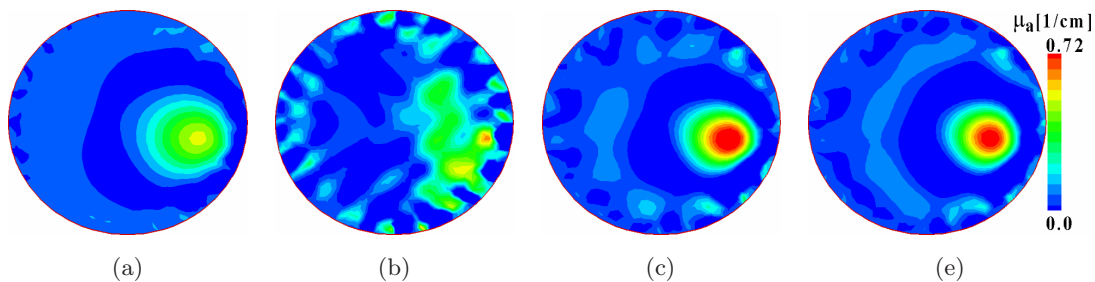


Fig. 6.   Intermediate reconstruction maps for the 4.1 cm-in-diameter tissue phantom. (a) The DA-based reconstruction. (b) The $S_2$ ERT-based reconstruction. (c) The $S_4$ ERT-based reconstruction. (d) The full ERT-based conventional scheme.

same reason as mentioned in the previous cases [see Fig. 6(b)], while the other two (DA-based and $S_4$ ERT-based codes) work very well to obtain the feasible intermediate solution $\mu^m$ that can be used to accelerate the full ERT-based reconstruction process [see Figs. 5(a) and 5(c)]. As a consequence, the

DA- and $S_4$ ERT-based codes lead to the speedup factors of 7.6 and 5.4 respectively. In terms of accuracy, the two hybrid codes, except for the $S_2$ ERT-based hybrid code, show similar results: both with $\rho = 0.81$ and $\delta = 0.64$ which indicates that the reconstructed map agrees well with the exact map

both with respect to the location and the reconstructed value of the object.

## 5.2. *Experimental study*

In addition to the numerical studies, we have started to explore the performance of our hybrid codes on experimental data. For the experimental studies, we use a tissue phantom with optical properties similar to those used for the numerical studies. A 4.1 cm-in-diameter cylindrical phantom is filled with a 1% intralipid fluid whose optical properties are known as $\mu_a = 0.023\,\text{cm}^{-1}$, $\mu_s' = 7.29\,\text{cm}^{-1}$ and $g = 0.73$. Also the cylinder phantom consists of a simple absorption inclusion rod (with the same scattering properties as the background), filled with Indian ink whose $\mu_a$ is not known. The cylinder is surrounded by two fiber-holding rings, each with 12 sources and 12 detectors spaced at $15°$ intervals. The data were acquired with a dynamic near-infrared optical tomographic (DYNOT) instrument. A more detailed description of the DYNOT instrument can be found in Ref. 33.

Since our instrument does not provide the absolute measurements due to the unknown calibration errors such as photon loss in fibers, we employed the following objective function[34–35]:

$$\phi = \frac{1}{2}\sum_{d=1}^{ND}\left\|\frac{M_{\text{tar},d}}{M_{\text{ref},d}}P_{\text{ref},d} - P_{\text{tar},d}\right\|^2, \qquad (20)$$

where the subscript $d$ denotes the number of measurements. $M_{\text{tar},d}$ and $M_{\text{ref},d}$ denote the measurements for the target medium of unknown optical properties and the reference medium of known optical properties, respectively. $P_{\text{ref},d}$ and $P_{\text{tar},d}$ are the corresponding forward predictions for the reference medium of known optical properties and the target medium of unknown optical properties, respectively.

We reconstructed the spatial distribution of the absorption coefficient in the cylinder by using the hybrid schemes. Since we do not know the exact value of the absorption coefficient of Indian ink, we just provide the correlation factor $\rho$ alone in Table 2 for a qualitative assessment of the reconstructed images to evaluate the performance of the codes. As shown in Fig. 6, the intermediate reconstruction results from the DA- and $S_4$ ERT-based reconstructions follow well the result obtained from the $S_8$ ERT-based conventional method. In terms of CPU time, we observed that the hybrid schemes accelerate the reconstruction process by a factor of six to eight. As in the numerical studies, the $S_2$ ERT-based reconstruction did not make the reasonable initial guess in this case. These results demonstrate that the DA- and $S_4$ ERT-based hybrid codes lead to significant time saving while keeping reasonable accuracy.

## 6. Conclusion

We introduced here the three DA-ERT hybrid codes: the DA-based hybrid code, the $S_2$ ERT-based hybrid code, and the $S_4$ ERT-based hybrid code. To evaluate the performance of the codes, we presented numerical and experimental studies by comparing the results of the hybrid codes to those of the $S_8$ ERT-based conventional code.

We showed that the hybrid schemes are very useful for reducing the reconstruction time. The DA-based hybrid code accelerates the reconstruction process up to 23 times. The $S_2$ ERT-based hybrid does not work well for most of the cases considered here, and the $S_4$ ERT-based hybrid code always performs well for all the cases considered in this work, leading to a speedup factor of 6.2.

## Acknowledgments

## References

1. L. C. Enfield, A. P. Gibson, J. C. Hebden, M. Douek, "Optical tomography of breast cancer — monitoring response to primary medical therapy," *Targ. Oncol.* DOI 10.1007/s11523-009-0115-z (2009).

2. S. C. Davis, H. Dehghani, J. Wang, S. Jiang, B. W. Pogue, K. D. Paulsen, "Image-guided diffuse optical fluorescence tomography implemented with Laplacian-type regularization," *Opt. Express* **15**, 4066–4082 (2007).

3. A. Corlu, R. Choe, T. Durduran, M. A. Rosen, M. Schweiger, S. A. Arridge, M. D. Schnall, A. G. Yodh,

"Three-dimensional *in vivo* fluorescence diffuse optical tomography of breast cancer in humans," *Opt. Express* **15**, 6696 (2007).

4. Y. Xu, H. L. Graber, R. L. Barbour, "Image correction algorithm for functional three-dimensional diffuse optical tomography brain imaging," *Appl. Opt.* **46**, 1693–1704 (2007).

5. D. K. Joseph, T. J. Huppert, M. A. Franceschini, D. A. Boas, "Diffuse optical tomography system to image brain activation with improved spatial resolution and validation with functional magnetic resonance imaging," *Appl. Opt.* **45**, 8142–8151 (2006).

6. D. A. Boas, K. Chen, D. Grebert, M. A. Franceschini, "Improving the diffuse optical imaging spatial resolution of the cerebral hemodynamic response to brain activation in humans," *Opt. Lett.* **29**, 1506 (2004).

7. J. C. Hebden, A. P. Gibson, T. Austin, R. M. Yusof, N. Everdell, D. T. Delpy, S. R. Arridge, J. H. Meek, J. S. Wyatt, "Imaging changes in blood volume and oxygenation in the newborn infant brain using three-dimensional optical tomography," *Phys. Med. Biol.* **49**, 1117–1130 (2004).

8. A. Y. Bluestone, G. S. Abdoulaev, C. Schmitz, R. Barbour, A. H. Hielscher, "Three-dimensional optical tomography of hemodynamics in the human head," *Opt. Express* **9**, 272 (2001).

9. A. H. Hielscher, A. D. Klose, A. Scheel, B. Moa-Anderson, M. Backhaus, U. Netz, J. Beuthan, "Sagittal laser optical tomography for imaging of rheumatoid finger joints," *Phys. Med. Biol.* **49**, 1147 (2004).

10. A. K. Scheel, M. Backhaus, A. D. Klose, B. Moa-Anderson, U. Netz, K. G. Hermann, J. Beuthan, G. A. Muller, G. R. Burmester, A. H. Hielscher, "First clinical evaluation of sagittal laser optical tomography for detection of synovitis in arthritic finger joints," *Ann. Rheum. Dis.* (2004).

11. Q. Zhang, H. Jiang, "Three-dimensional diffuse optical tomography of simulated hand joints with a $64 \times 64$-channel photodiodes-based optical system," *J. Opt. A Pure Appl. Opt.* **7**, 224–231 (2005).

12. A. H. Hielscher, "Optical tomographic imaging of small animals," *Curr. Opin. Biotechnol.* **16**, 79–88 (2005).

13. H. Xu, R. Springett, H. Dehghani, B. W. Pogue, K. D. Paulsen, J. F. Dunn, "Magnetic-resonance-imaging coupled broadband near-infrared tomography system for small animal brain studies," *Appl. Opt.* **44**, 2177–2188 (2005).

14. A. Y. Bluestone, M. Stewart, B. Lei, I. S. Kass, J. Lasker, G. S. Abdoulaev, A. H. Hielscher, "Three-dimensional optical tomographic brain imaging in small animals: Part I. Hypercapnia," *J. Biomed. Opt.* **9**, 1046–1062 (2004).

15. A. Y. Bluestone, M. Stewart, J. Lasker, G. S. Abdoulaev, A. H. Hielscher, "Three-dimensional optical tomographic brain imaging in small animals: Part II. Unilateral carotid occlusion," *J. Biomed. Opt.* **9**, 1063–1073 (2004).

16. S. R. Arridge, "Optical tomography in medical imaging," *Inverse Problems* **15**, R41–93 (1999).

17. A. H. Hielscher, A. D. Klose, K. M. Hanson, "Gradient-based iterative image reconstruction scheme for time-resolved optical tomography," *IEEE Trans. Med. Imaging* **18**, 262–271 (1999).

18. Y. Q. Yao, Y. Wang, Y. L. Pei, W. W. Zhu, R. L. Barbour, "Frequency-domain optical imaging of absorption and scattering distributions by Born iterative method," *J. Opt. Soc. Am. A* **14**, 325–342 (1997).

19. J. C. Ye, K. J. Webb, C. A. Bouman, R. P. Millane, "Optical diffusion tomography by iterative-coordinate descent optimization in a Bayesian framework," *J. Opt. Soc. Am. A* **16**, 2400–2412 (1999).

20. J. Ripoll, V. Ntziachristos, "Iterative boundary method for diffuse optical tomography," *J. Opt. Soc. Am. A* **20**, 1103–1110 (2003).

21. A. D. Klose, A. H. Hielscher, "Quasi-Newton methods in optical tomographic image reconstruction," *Inverse Problems* **19**, 309–387 (2003).

22. R. Roy, E. M. Sevick-Muraca, "Active constrained truncated Newton method for simple-bound optical tomography," *J. Opt. Soc. Am. A* **17**, 1627–1641 (2000).

23. X. Intes, V. Ntziachristos, J. P. Culver, A. Yodh, B. Chance, "Projection access order in algebraic reconstruction technique for diffuse optical tomography," *Phys. Med. Biol.* **47**, N1–10 (2002).

24. R. Ren, G. Bal, A. H. Hielscher, "Frequency domain optical tomography with the equation of radiative transfer," *SIAM J. Sci. Comput.* **28**, 1463–1489 (2006).

25. H. K. Kim, A. Charette, "A sensitivity function-based conjugate gradient method for optical tomography with the frequency-domain equation of radiative transfer," *J. Quantum Spectrosc. Radiat. Transfer* **104**, 24–39 (2007).

26. M. Schweiger, S. Arridge, I. Nassila, "Gauss–Newton method for image reconstruction in diffuse optical tomography," *Phys. Med. Biol.* **50**, 2365–2386 (2005).

27. A. H. Hielscher, A. E. Alcouffe, R. L. Barbour, "Comparison of finite-difference transport and diffusion calculations for photon migration in homogeneous and heterogeneous tissues," *Phys. Med. Biol.* **43**, 1285–1302 (1998).

28. L. G. Henyey, L. J. Greenstein, "Diffuse radiation in the galaxy," *Astrophys.* **90**, 70 (1941).

29. A. Klose, V. Ntziachristos, A. H. Hielscher, "The inverse source problem based on the radiative transfer equation in optical molecular imaging," *J. Comput. Phys.* **202**, 323–345 (2005).

30. Y. Saad, "GMRES: A generalized minimum residual algorithm for solving nonsymmetric linear systems," *SIAM J. Sci. Stat. Comput.* **7**, 856–869 (1986).

31. J. Nocedal, S. J. Wright, *Numerical Optimization*, Spinger-Verlag, New York (1999).

32. O. M. Alifanov, *Inverse Heat Transfer Problems*, Springer-Verlag, Berlin (1994).

33. C. H. Schmitz, M. Löcker, J. M. Lasker, A. H. Hielscher, R. L. Barbour, "Instrumentation for fast functional optical tomography," *Rev. Sci. Instrument.* **73**, 429–439 (2002).

34. A. Y. Bluestone, M. Stewart, B. Lei, I. S. Kass, J. Lasker, G. S. Abdoulaev, A. H. Hielscher, "Three-dimensional optical tomographic brain imaging in small animals: Part I. Hypercapnia," *J. Biomed. Opt.* **9**, 1046–1062 (2004).

35. Y. Pei, H. L. Graber, R. L. Barbour, "Influence of systematic errors in reference states on image quality and on stability of derived information for DC optical imaging," *Appl. Opt.* **40**, 5755–5769 (2001).